

# Universal Model for the Turn-On Dynamics of Superconducting Nanowire Single-Photon Detectors


Kathryn L. Nicolich<sup>1,\*</sup>, Clinton Cahall,<sup>2</sup> Nurul T. Islam,<sup>1</sup> Gregory P. Lafyatis,<sup>1</sup> Jungsang Kim,<sup>2,3</sup> Aaron J. Miller,<sup>4</sup> and Daniel J. Gauthier<sup>1</sup>

<sup>1</sup>*Department of Physics, The Ohio State University, Columbus, Ohio 43210, USA*

<sup>2</sup>*Department of Electrical and Computer Engineering, Duke University, Durham, North Carolina 27708, USA*

<sup>3</sup>*IonQ, Inc., College Park, Maryland 20740, USA*

<sup>4</sup>*Quantum Opus LLC, Novi, Michigan 48375, USA*

 (Received 2 November 2018; revised manuscript received 11 July 2019; published 11 September 2019)

We describe an electrothermal model for the turn-on dynamics of superconducting nanowire single-photon detectors (SNSPDs). By extracting a scaling law from a well-known electrothermal model of SNSPDs, we show that the rise time of the readout signal encodes the photon number as well as the length of the nanowire with scaling  $t_{\text{rise}} \propto \sqrt{\ell/n}$ . We show that these results hold regardless of the exact form of the thermal effects. This explains how SNSPDs have an inherent photon-number-resolving capability. We experimentally verify the photon-number dependence by collecting waveforms for different photon numbers, rescaling them according to our predicted relation, and performing statistical analysis that shows that there is no statistical significance between the rescaled curves. Additionally, we use our predicted dependence of the rise time on the detector length to provide further insight into previous theoretical work by other authors. By assuming a specific thermal model, we predict that rise time will scale with the bias current,  $t_{\text{rise}} \propto \sqrt{1/I_b}$ . We fit this model to experimental data and find that  $t_{\text{rise}} \propto 1/(n^{0.52 \pm 0.03} I_b^{0.63 \pm 0.02})$ , which suggests that further work is needed to better understand the bias-current dependence. This work gives insights into the nonequilibrium dynamics of thin superconducting films exposed to electromagnetic radiation.

DOI: [10.1103/PhysRevApplied.12.034020](https://doi.org/10.1103/PhysRevApplied.12.034020)

## I. INTRODUCTION

Superconducting nanowire single-photon detectors (SNSPDs) are widely used in quantum optics and quantum information science because of their high efficiency over a wide range of wavelengths, fast reset times, low timing jitter, and low dark-count rates, and the typical lack of afterpulsing [1,2]. Despite the widespread use of these detectors, their dynamics are still not fully understood.

A qualitative picture of SNSPD operation involves one or more photons absorbed by the device simultaneously that create resistive regions in the nanowire, known as hot spots, which divert current out of the detector and into the readout circuit, constituting a detection event. A complete quantitative model requires knowledge of the spatiotemporal dynamics of the nonequilibrium distribution of quasiparticles in the superconductor and its interaction with the readout electronics. The understanding of the microscopic details of these devices is rapidly advancing [3]; however, electrothermal models of SNSPDs frequently have more parameters than measurable constraints [4,5]. Hence,

similar forms of behavior may be fitted using different sets of model parameters, thus potentially obscuring the physical principles underlying SNSPD behavior.

Here, we describe a simple SNSPD model that captures the essential physics of the link between hot-spot growth and features of the rising edge of the electrical readout pulse. The model identifies a “universal curve” for the electrical signal. Converting this model to physical units requires using only two scale parameters, which can be determined experimentally, and gives a simple relation between the microscopic SNSPD parameters and the readout signal. Using scaling relations derived from our model equations, we explain the recent demonstration of multi-photon resolution in a conventional SNSPD [6]. Further, we predict the scaling of the turn-on time with nanowire length  $\ell$  and find results consistent with a previous prediction that relies on a more complex model. Finally, by refining our model in a way suggested by the work of Kerman *et al.* [5], we predict the specific shape of the rising edge of a readout pulse and the dependence of the rise time on the bias current  $I_b$  of the detector. We claim that our theoretical predictions hold regardless of the detector material and we compare with experiments

\*nicolich.1@osu.edu

performed using a detector made from a proprietary amorphous superconductor in a class similar to that of WSi and MoSi, as well as results from the literature on NbN. We find good agreement between the model predictions and experimental measurements.

## II. DETECTION MODEL

A typical high-detection-efficiency SNSPD consists of a thin (thickness approximately 5–10 nm) and narrow (width  $w \sim 100$  nm) superconducting film shaped into a meander that matches the optical-field mode of the photon source as illustrated in Fig. 1(a). Electrically, we treat the SNSPD using lumped circuit elements coupled to a readout circuit, shown in Fig. 1(b). The detector bias current splits between two pathways to ground: the current  $I_{\text{det}}$  passing through the SNSPD and the signal current  $I_s$  passing through the readout-circuit load resistor  $R_L$ . The SNSPD is treated as a kinetic inductance  $L_k$ , connected in series with a parallel combination of a time-dependent resistance,  $R_N(t)$ , and a switch. The resistive part of the nanowire due to photon detection is represented using  $R_N(t)$  and the switch being closed represents the entire nanowire being in the superconducting state. In Ginzburg-Landau theory,  $L_k$  depends on  $I_{\text{det}}$ . The variation is essentially constant when the current is below approximately 90% of the depairing current and decreases rapidly as  $I_{\text{det}}$  approaches the depairing current from below [7]. For most present-day SNSPDs,  $I_{\text{det}}$  is well enough below the depairing current that taking  $L_k$  constant is a good approximation and here we assume that to be the case. This approximation is discussed further in Appendix A. In the absence of photons, the nanowire is in thermal equilibrium with the substrate at temperature  $T_o < T_c$ , where  $T_c$  is the superconducting

critical temperature at zero bias, and the switch is closed ( $I_{\text{det}} = I_b, I_s = 0$ ).

A detection event begins with the absorption of a photon by the nanowire with an energy much greater than the superconducting gap energy [Fig. 1(a)(i)], giving rise to a hot spot. We use the so-called hot-spot mechanism to describe the operation of the detector. While there continues to be some uncertainty of the appropriateness of this model during the very short time during the initiation of a detection event [8–12], it does predict many of the experimental observations across the literature. For the purposes of this paper, we consider only the dynamics after the hot spot has already grown across the entire cross-section area of the nanowire [13]. Note that throughout this work we use the term “hot spot” to refer to the normal region as it grows and shrinks due to Joule heating, in contrast with the localized resistive region present immediately following photon absorption, before Joule heating takes place. The hot spot spreads rapidly due to quasiparticle diffusion and extends across the width of the nanowire [Fig. 1(a)(ii)], giving rise to a resistive (normal) wire segment with resistance  $R_{\text{HS}}$ . In the lumped-element circuit model, the switch is now open.

The hot spot continues to grow along the length of the wire due to Joule heating from current  $I_{\text{det}}$  passing through the normal region and this growth is characterized by a phase-front velocity  $v = v(I_{\text{det}})$  at its boundaries [Fig. 1(a)(iii–iv)]. This treatment is widely used to describe SNSPD dynamics and is appropriate as long as the thermal healing length  $L_H$  is much smaller than the length of the hot spot. For NbN-based detectors,  $L_H = 20$  nm; therefore, this approximation is valid for all but the very early initial stages of hot-spot development [4,5]. As the resistive region grows, more current is shunted into the readout circuit, resulting in the rising edge of the electrical pulse shown in Fig. 1(c). As more current is shunted out of the detector, the hot-spot growth slows and stalls at a steady-state current  $I_{\text{ss}}$ . (Some authors call this the retrapping current [14,15].)

Here, we focus on the time interval during hot-spot growth and decay up until hot-spot collapse, which corresponds to the rising edge of the electrical pulse. This sequence of events takes place on a short time scale, typically less than 1 ns. Previously, the rising edge of the readout signal has been described as an exponential growth with time constant  $L_k/R_{\text{HS}}$  [16], where  $R_{\text{HS}} \sim 10^3 \Omega$  is constant during the presence of the hot spot. However, as we show below, this is not an accurate picture and it leads to incorrect conclusions about the detector turn-on dynamics.

Shortly after its growth stalls, the hot spot collapses as cooling to the substrate dominates over Joule heating, as shown in Fig. 1(a)(v). Once the nanowire returns to the superconducting state, the switch in the lumped-element circuit model is closed and the readout pulse begins to

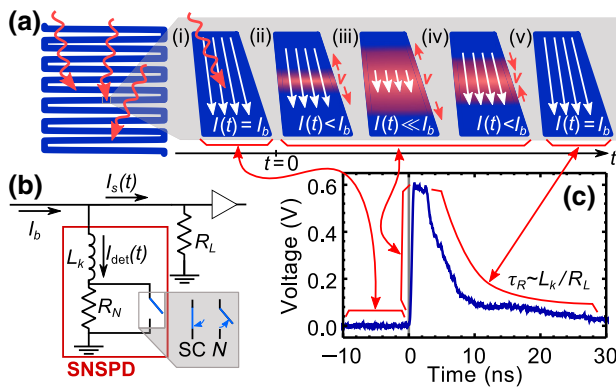


FIG. 1. (a) A depiction of an SNSPD meander with incident photons. (a)(i) An illustration of a region of the SNSPD near an incident and absorbed photon. (a)(ii–v) The progression of hot-spot formation, growth, and decay, which is described using the front velocity  $v$ . (b) The lumped-element circuit diagram of an SNSPD and the readout. (c) An example SNSPD readout pulse. The vertical gray line marks  $t = 0$ .

decay exponentially on a time scale governed by the time it takes for the current to return to the inductor [Eq. (2) with  $R_{\text{HS}} = 0$ ], which has a  $1/e$  recovery time of  $\tau_r = L_k/R_L$ . Note that during the decay of the pulse, both  $L_k$  and  $R_L$  are constant. For high-speed readout circuits,  $R_L$  is often  $50 \Omega$ , so that  $\tau_r$  is tens of nanoseconds—much longer than the rise time of  $I_s$ .

The dynamics of the coupled system during a detection event are governed by the interplay between the superconducting nanowire and the readout circuit, which we describe using an electrothermal model given by

$$\frac{dR_{\text{HS}}}{dt} = 2 \frac{R_{\text{max}}}{\ell} v(I_{\text{det}}), \quad R_{\text{HS}} \geq 0, \quad (1)$$

$$L_k \frac{dI_{\text{det}}}{dt} + nR_{\text{HS}}I_{\text{det}} = (I_b - I_{\text{det}})R_L, \quad (2)$$

these equations being valid immediately after the initiation of a detection event, with initial conditions  $R_{\text{HS}}(0) = 0$  and  $I_{\text{det}}(0) = I_b$ . Here,  $R_{\text{max}}$  is the resistance of the nanowire when its total length  $\ell$  is in the normal state, which occurs when  $T > T_c$  at  $I_b = 0$  or  $I_b \gg I_{\text{sw}}$  at  $T = 0$ , where  $I_{\text{sw}}$  is the switching current. Thus  $R_{\text{max}}/\ell$  is the resistance per unit length of the nanowire and Eq. (1) expresses the above description of hot-spot growth. The factor of 2 accounts for the two fronts that bound a hot spot. Physically,  $R_{\text{HS}} > 0$ , but the system of equations allows for unphysical solutions arising from the superconductivity transition of the hot spot. Keeping the solution in the physical domain requires setting  $R_{\text{HS}} = 0$  when  $R_{\text{HS}}$  falls below zero in solving the system of equations. Here, we assume that  $v(I_{\text{det}})$  only depends on the present value of  $I_{\text{det}}$  and not on the size or history of the hot spot. The physics of a propagating superconducting-normal boundary, traveling at a phase velocity  $v(I_{\text{det}})$ , for long narrow superconductors, has been studied extensively because of its importance in understanding quenching of superconducting magnets [17]. In the latter half of this work, we use a particular form of  $v(I_{\text{det}})$  that is well suited to most SNSPDs.

Equation (2) is Kirchhoff's voltage law for the SNSPD-load resistor loop. We allow for the possibility that  $n$  photons are absorbed by the film simultaneously, as might happen when illuminating the nanowire with a short-duration multiphoton wave packet. We assume that each absorbed photon generates a hot spot with identical behavior and that they do not overlap spatially. This is appropriate for a small number of hot spots with typical stalled hot-spot maximum lengths (approximately  $1 \mu\text{m}$ ) and typical values of  $\ell$  (approximately  $500 \mu\text{m}$ ) [4]. The total nanowire resistance is then given by  $R_N(t) = nR_{\text{HS}}(t)$ . While the hot spots do not interact directly in our model, they are coupled indirectly through the electrothermal interaction.

### III. CHARACTERISTIC SCALES

To explore the effects of various parameters on detector rise times, we rescale Eqs. (1) and (2). There are two time scales inherent in this system of equations,  $\tau_r$  and  $t_{\text{ch}}$ , the latter of which is the characteristic time scale for the dynamics related to the rising edge of the readout pulse. Because we are interested in studying this regime, we rescale Eqs. (1) and (2), taking  $t_{\text{ch}}$  to be the dominant time scale. We introduce the dimensionless quantities  $\tilde{t} = t/t_{\text{ch}}$ ,  $\tilde{\tau}_r = \tau_r/t_{\text{ch}}$ ,  $\tilde{R}(\tilde{t}) = R_{\text{HS}}(t)/R_{\text{ch}}$ ,  $\tilde{R}_{\text{max}} = R_{\text{max}}/R_{\text{ch}}$ ,  $\tilde{I}(\tilde{t}) = I_{\text{det}}(t)/I_b$ , and  $\tilde{v}(\tilde{I}) = v(I_{\text{det}})/v_b$ , where  $v_b = v(I_b)$  is the phase-front velocity at the start of hot-spot formation. Here, the characteristic resistance  $R_{\text{ch}}$  represents the maximum resistance attained by a single hot spot and it and  $t_{\text{ch}}$  are given, respectively, by

$$R_{\text{ch}} = \sqrt{\frac{4v_b R_{\text{max}} L_k}{n\ell}}, \quad (3)$$

$$t_{\text{ch}} = \frac{2L_k}{nR_{\text{ch}}} = \sqrt{\frac{\ell L_k}{nv_b R_{\text{max}}}}. \quad (4)$$

Substituting these expressions into Eqs. (1) and (2) results in the dimensionless set of equations

$$\frac{d\tilde{R}}{d\tilde{t}} = \tilde{v}(\tilde{I}), \quad \tilde{R} \geq 0, \quad (5)$$

$$\frac{d\tilde{I}}{d\tilde{t}} + 2\tilde{R}\tilde{I} = \frac{1}{\tilde{\tau}_r}(1 - \tilde{I}). \quad (6)$$

In the rescaling of Eqs. (3) and (4), the dependence on the photon number  $n$  is the unique choice for eliminating the explicit  $n$  dependence in Eqs. (1) and (2). There is still a “hidden” dependence in that systems with different numbers of photons will have different values of  $\tilde{\tau}_r$ .

For typical SNSPDs, the turn-on dynamics are much faster than the recovery time  $\tau_r$ , such that  $\tilde{\tau}_r \gg 1$  ( $nR_{\text{ch}} \gg 2R_L$ ), and it is possible to neglect the right-hand side of Eq. (6). Assuming that we operate in this domain, the coupled equations become

$$\frac{d\tilde{R}}{d\tilde{t}} = \tilde{v}(\tilde{I}), \quad \tilde{R} \geq 0, \quad (7)$$

$$\frac{d\tilde{I}}{d\tilde{t}} + 2\tilde{R}\tilde{I} = 0, \quad (8)$$

with initial conditions  $\tilde{R}(\tilde{t} = 0) = 0$  and  $\tilde{I}(\tilde{t} = 0) = 1$ . Here,  $\tilde{v}(\tilde{I})$  plays the role of a driving term for the system of equations. We first consider the nanowire operating at a specific bias current  $I_b$ . The phase-front velocity is taken to be some (perhaps unknown) function of the detector current  $v(I)$ . However, for all cases that have the same

bias current  $I_b$ , the scaled velocity function  $\tilde{v}(\tilde{I})$  is identical—these cases are all described by exactly the same scaled equations above and hence have exactly the same scaled solutions for  $\tilde{I}(\tilde{t})$  and  $\tilde{R}(\tilde{t})$ . In particular, the relative values for the characteristic time scale for the turn-on dynamics  $t_{\text{ch}}$  are independent of the specific form of  $\tilde{v}$ .

Therefore, for a detector operating at a specified  $I_b$ , we can directly relate the signal for a multiphoton event to that of a single-photon event by explicitly expressing the solution of Eqs. (7) and (8) for the scaled current in terms of the actual physical quantities for the two cases:

$$I_1(t) = I_n(t/\sqrt{n}). \quad (9)$$

Thus, the absorbed photon number  $n$  is encoded within the turn-on dynamics, which can be revealed by measuring the 10%–90% signal rise time or the maximum value of  $dI_{s,n}/dt \propto \sqrt{n} dI_{s,1}/dt$ . This explains the recent experimental findings of Cahall *et al.* [6].

To compare our theoretical predictions with experimental observations, we collect waveforms from a proprietary amorphous device for optical wave packets with  $n = 1, 2$ , and 3 photons in the same manner as in Ref. [6], using a higher-bandwidth readout circuit to minimize signal distortion, and rescale them using the same principle as in Eq. (9) (for the experimental details, see Appendices B and C). In Fig. 2(a), we show the rising edges of the waveforms collected at the readout. Figure 2(b) shows the waveforms after rescaling by  $\sqrt{n}$ , where it is seen that the waveforms appear to fall on a single curve. This phenomena is more apparent when examining the derivatives of the waveforms, which are shown in Fig. 2(c) and rescaled in Fig. 2(d). The difference at  $t = 0$  in the derivative curves is statistically significant. In contrast, there is

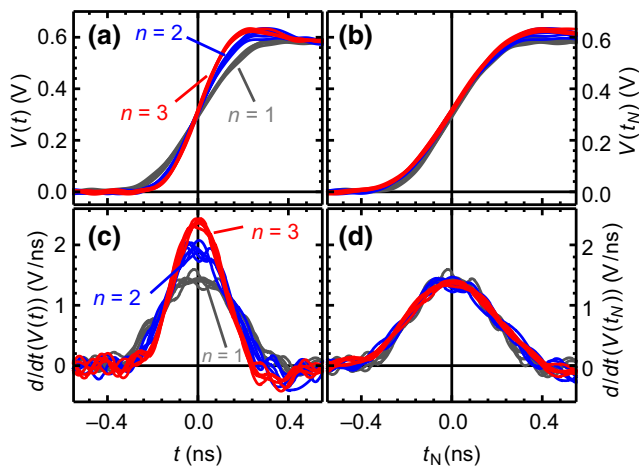


FIG. 2. (a) The rising edges of the  $n = 1, 2$ , and 3 traces (gray, blue, and red) and (b) with  $t_N = t/\sqrt{n}$ , as well as their derivatives with respect to time (c) and (d).

no statistical significance between the rescaled derivative curves at  $t = 0$  (for the details of the statistical analysis, see Appendix D). Therefore, we claim that rescaling the traces by  $\sqrt{n}$  reveals a universal curve that is independent of the photon number. Ringing from our amplifier distorts this effect somewhat beyond  $t_N = 0.4$  ns in the rescaled curves.

Recent work by Smirnov *et al.* [15] provides a second test of our model. They modeled and experimentally studied the effect of the detector length on single-photon pulse rise times for SNSPDs. They presented a two-temperature (quasiparticle and/or phonon distribution) model described by five coupled differential equations, which was numerically solved to predict the readout-signal rise times. They tested their predictions by comparing signals from detectors with different values of  $\ell$ . The authors argued, qualitatively, that the dependence of rise time on  $\ell$  should be nonlinear for  $\ell > 20 \mu\text{m}$  and their model equations confirm this. While we cannot make absolute estimates of detector rise times, we can make a stronger claim of the nature of the nonlinear dependence on  $\ell$ . Detectors differing only in length (and operated at the same bias current) will all be described in our approach by Eqs. (7) and (8). In Eq. (4),  $L_k$  and  $R_{\text{max}}$  are proportional to  $\ell$ . Therefore, we predict that  $t_{\text{ch}}$ , and hence the detector rise time, should scale as  $\sqrt{\ell}$ . We fit the model calculations of Smirnov *et al.* [15] to  $g + h\ell^{1/2}$ , allowing  $g$  and  $h$  to be fit parameters, and find that  $g = 15.1 \pm 0.8$  ps and  $h = 15.01 \pm 0.04$  ps/ $\mu\text{m}^{1/2}$ , with a reduced chi-square statistic of approximately 1 as shown in Fig. 3 (for more information, see Appendix E). Our prediction for the scaling of the rise time on  $\ell$  and  $n$  does not require a solution to the differential Eqs. (1) and (2), but is based only on the rescaling of the equations in physical units, Eqs. (3) and (4). Thus, we conclude that these scaling results are due to the thermoelectric coupling and do not depend on the microscopic physics that defines the functional dependence of  $v$  on  $I_{\text{det}}$ .

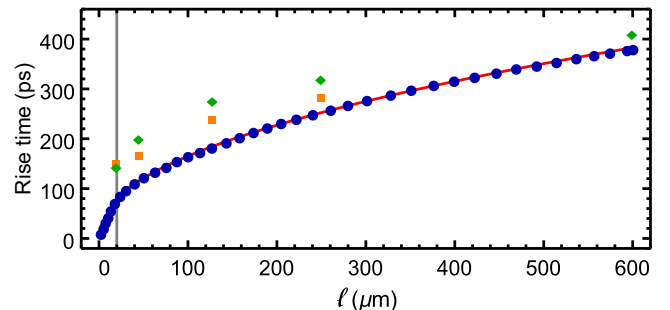


FIG. 3. Our prediction  $t_{\text{rise}} \propto \sqrt{\ell}$  (red curve) compared with the theoretical predictions from Smirnov *et al.* [15] (blue dots), alongside their experimental results for NbN on Si/Si<sub>3</sub>N<sub>4</sub> (green diamonds) and Si/SiO<sub>2</sub> (orange squares). We fit their theoretical predictions for values  $> 20 \mu\text{m}$  (gray vertical line).



#### IV. UNIVERSAL MODEL

More detailed information may be gleaned from Eq. (4) by assuming a specific functional form for  $\tilde{v}(\tilde{I})$ . We follow Kerman *et al.* [5] by using an approximate solution to the phase-front velocity originally derived by Broom and Rhoderick [18], which in physical unscaled units is as follows:

$$v(I) = \sqrt{2}v_o \frac{I^2/I_{ss}^2 - 1}{\sqrt{I^2/I_{ss}^2 - 1/2}}. \quad (10)$$

Here,  $v_o = \sqrt{\alpha\kappa/d}/c$ , where  $\kappa$ ,  $c$ , and  $d$  are the thermal conductivity, the specific heat per unit volume, and the thickness of the nanowire, respectively, and  $\alpha$  is the heat-conductivity coefficient for cooling to the substrate. Note that  $v(I_{ss}) = 0$  from Eq. (10), as discussed qualitatively above. An important quantity in studying these problems is the Stekly parameter, which describes the relative magnitudes of Joule heating and cooling to the substrate:  $s = 2(I_{sw}/I_{ss})^2$  [5,17]. For most SNSPDs,  $s$  is large, as it is for our detector with  $s = 300$ . A device is usually biased near  $I_{sw}$ ; therefore, over most of the rise time, Eq. (10) may be approximated as the linear relation  $v(I) = \sqrt{2}v_o I/I_{ss}$  and, importantly,  $v_b = \sqrt{2}v_o I_b/I_{ss}$ . Under these assumptions and using Eq. (4), we obtain the additional scaling relation  $t_{ch} \propto 1/\sqrt{I_b}$ . We test this prediction against our experimental observations below.

Taking this linear thermal model, Eqs. (7) and (8) may be solved in terms of elementary functions given by

$$\tilde{I}(\tilde{t}) = \text{sech}^2(\tilde{t}), \quad (11)$$

$$\tilde{R}(\tilde{t}) = \tanh(\tilde{t}), \quad \tilde{t} \geq 0, \quad (12)$$

where we continue to assume that the term proportional to  $1/\tilde{\tau}_r$  in Eq. (6) can be ignored. For comparing to experiment, it is useful to restate Eq. (11) in terms of the readout signal  $\tilde{I}_s = \tanh^2(\tilde{t})$  and we have done so below. Note that this form of  $\tilde{v}$  does not allow for detector reset and hence only describes the SNSPD turn-on dynamics.

We find that the time at which  $\tilde{I}_s$  ( $\tilde{R}$ ) reaches a value of 1/2 is given by  $\tilde{t}_{1/2} \sim 0.881$  ( $\sim 0.549$ ), consistent with the scaling behavior discussed above for a generic thermal model. To directly compare this model to experiment, only knowledge of  $I_b$  and two scale parameters is needed (for more information on extracting scale parameters, see Appendices F and G). Therefore, for large  $\tau_r$  and  $s$ , Eqs. (11) and (12) constitute a universal model for SNSPD turn-on dynamics.

We compare the predictions of the exact model of Ref. [5] using Eqs. (5), (6), and (10) without approximation, and our universal model given by Eqs. (11) and (12) in Fig. 4. Here, we show the temporal evolution of  $\tilde{I}_s = 1 - \tilde{I}$  and  $\tilde{R}$  for three different operating conditions: (1) one- and (2) three-photon detection events for a typical value

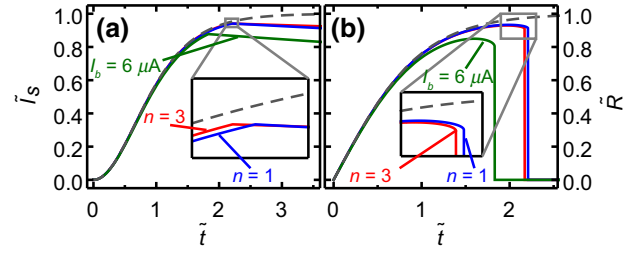


FIG. 4. A comparison of the exact [Eqs. (5) and (6)] and universal model solutions [Eqs. (11) and (12), dashed line] for (a) the current and (b) the resistance. Here, the parameters for the exact model are as follows: blue line,  $n = 1$ ,  $I_b = 12.5 \mu\text{A}$ ; red line,  $n = 3$ ,  $I_b = 12.5 \mu\text{A}$ , green line,  $n = 1$ ,  $I_b = 6 \mu\text{A}$ . For all curves,  $R_L = 50 \Omega$ ,  $L_k = 0.824 \mu\text{H}$ ,  $v_o = 60 \text{ pm/ns}$ ,  $R_{sq} = 461 \Omega$ ,  $w = 70 \text{ nm}$ , and  $I_{ss} = 1.04 \mu\text{A}$ .

of  $I_{ss} \ll I_b \lesssim I_{sw}$ ; and (3) a one-photon event at  $I_b \sim 6I_{ss}$ , which is a value smaller than that used in typical experiments. For all cases, the universal model agrees well with the exact model up to  $\tilde{t} \sim 2$ . Beyond this time, a distinct change in slope in the curves for  $\tilde{I}$  predicted by the exact model appears due to the detector returning to the superconducting state ( $\tilde{R}$  jumps abruptly to zero). For all curves up to  $\tilde{t} = 1$ , the difference between the exact and universal models is  $< 3\%$  for  $\tilde{I}$  and  $< 4\%$  for  $\tilde{R}$  and the small disagreement is greatest for lower  $I_b$ , as expected. Thus, the universal model is an excellent tool for understanding typical SNSPD turn-on dynamics.

#### V. EXPERIMENTAL RESULTS

To further explore the utility of our universal model, we use it to fit to experimental data to determine  $t_{ch}$  for our detector. We record  $I_s$  for various values of  $n$  with  $I_b \sim I_{sw}$  and for various values of  $I_b$  with  $n = 1$  (for more information, see Appendix F). We then fit the data using the dimensional form of Eq. (11), to find  $t_{ch}$  for each data set. The results are shown in Fig. 5. Considering only the photon-number data with  $I_b = 10.6I_{ss}$ , we expect  $t_{ch} = A/n^a$  with  $a = 0.5$ . We find that  $A = 295 \pm 5 \text{ ps}$  and

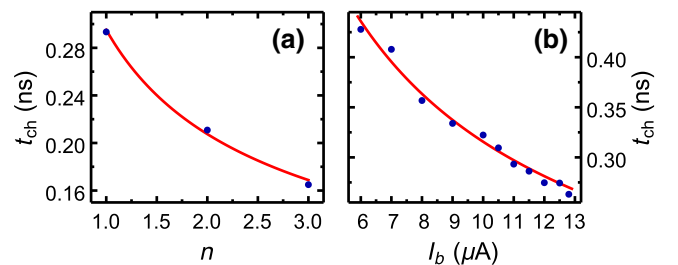


FIG. 5. The experimental values of  $t_{ch}$  (blue dots) extracted by fitting with our linear model vs (a)  $n$  with  $I_b = 11 \mu\text{A}$  and (b)  $I_b$  with  $n = 1$ , as well as their fits (red curves) to the model  $t_{ch} = A/n^a$  or  $t_{ch} = B/(I_b)^b$ , respectively.

$a = 0.51 \pm 0.03$ . Therefore, the scaling is consistent with our universally predicted scaling. From  $A$  and other independently measured parameters (see Appendix G), we find that  $v_0 = 96 \pm 3$  m/s. This value of  $v_0$  is smaller than, but of the order of, that found for NbN-based SNSPDs [19] and is consistent with the slower turn-on and turn-off dynamics of SNSPDs based on the amorphous superconducting thin film considered here.

In contrast, considering only the bias-current data with  $n = 1$ , we expect  $t_{\text{ch}} = B/(I_b)^b$  with  $b = 0.5$ ; however, we find that  $B = 1.35 \pm 0.08$  ps  $\text{A}^{1/2}$  and  $b = 0.63 \pm 0.03$ . From  $B$ , we predict that  $v_0 = 50 \pm 5$  m/s. We also simultaneously fit all data using  $t_{\text{ch}} = C/(n^c I_b^d)$  and find that  $C = 1.36 \pm 0.07$  ps  $\cdot \text{A}^{1/2}$ ,  $c = 0.52 \pm 0.03$ ,  $d = 0.63 \pm 0.02$ , and  $v_0 = 50 \pm 6$  m/s. In both cases, the dependence of  $I_b$  on  $t_{\text{ch}}$  is inconsistent with our predicted value. The inconsistency may be due to some physics not captured in the model proposed in Ref. [5]. It may also be due to high measured dark counts for higher  $I_b$  measured in this detector, which may skew  $t_{\text{ch}}$  to lower values at higher  $I_b$  (see Appendix G). Finally, it may be related to distortions in the waveform caused by the amplifier, as discussed above.

## VI. CONCLUSION

In conclusion, we derive a universal model for the turn-on dynamics of SNSPDs that identifies characteristic time and resistance scales, which is used to predict the observed detector behavior. Even though there are many seemingly independent device parameters, they contribute to  $t_{\text{ch}}$  and  $R_{\text{ch}}$  in a highly dependent manner. Most importantly, this model explains the multiphoton resolution observed recently in SNSPDs. Additionally, we make further predictions on the effect of  $\ell$  and  $I_b$  on detector rise times and find good agreement, although our results for the latter suggest that more corrections might be needed for the model from Ref. [5]. These observations should greatly advance our understanding of the nonequilibrium dynamics of thin superconducting films exposed to light.

## ACKNOWLEDGMENTS

We gratefully acknowledge discussions of this work with Karl Berggren and Sae Woo Nam, and the financial support of the Office of Naval Research Multidisciplinary University Research Initiative program on Wavelength-Agile Quantum Key Distribution in a Marine Environment (Grant No. N00014-13-1-0627) and the NASA program on Superdense Teleportation (Grant No. NNX13AP35A).

## APPENDIX A: DEPENDENCE OF KINETIC INDUCTANCE ON DEVICE CURRENT

The kinetic inductance  $L_k$  of a superconducting nanowire is a function of the current density in the nanowire. Clem and Kogan [7] have shown theoretically

that near the superconductor's depairing current,  $L_k$  can vary by a large ( $> 1/2$ ) fraction from its low-current value. Santavica *et al.* [20] found experimentally that variations  $\leq 10\%$  are typical over the entire range of current values for which their nanowires remained superconducting. Similarly, we measured a variation of 8% in a WSi device [21]. In integrating Eqs. (7) and (8), we assume that  $L_k$  is constant. This should lead to a small error in the pulse-shape predictions for the initial part of the detector signal when the nanowire current is large and decreasing and its kinetic inductance is changing. This effect is below our present experimental sensitivity.

By contrast, the scaling relations with the photon number and the nanowire length are entirely unaffected by any kinetic inductance dependence on current. To see this, we begin by defining the normal state resistance and kinetic inductance per unit length of the nanowire:  $\mathcal{R} = R_{\text{max}}/\ell$  and  $\mathcal{L}_k(I) = L_k(I)/\ell$ , respectively. Here, the kinetic inductance is allowed to depend on the detector current. The model given in Eqs. (1) and (2) may be rewritten as follows:

$$\frac{dR_{\text{HS}}(t)}{dt} = 2\mathcal{R}v[I_{\text{det}}(t)], \quad R_{\text{HS}} \geq 0, \quad (\text{A1})$$

$$\ell\mathcal{L}_k[I_{\text{det}}(t)]\frac{dI_{\text{det}}(t)}{dt} + nR_{\text{HS}}(t)I_{\text{det}}(t) = 0. \quad (\text{A2})$$

Consistent with the above treatment, the right-hand side of Eq. (A2) is set equal to 0. We define the scaled variables  $\tau$ ,  $r$ , and  $i$  to arrive at the following scaling relations:

$$t = \sqrt{\frac{2n}{\ell}} \tau, \quad (\text{A3})$$

$$R_{\text{HS}}(t) = \sqrt{2n\ell} r(\tau), \quad (\text{A4})$$

$$I_{\text{det}}(t) = i(\tau). \quad (\text{A5})$$

In the scaled variables, Eqs. (A1) and (A2) become

$$\frac{dr(\tau)}{d\tau} = \mathcal{R}v[i(\tau)], \quad 0 \leq R_{\text{HS}}, \quad (\text{A6})$$

$$\mathcal{L}_k[i(\tau)]\frac{di(\tau)}{d\tau} + r(\tau)i(\tau) = 0. \quad (\text{A7})$$

The initial conditions for this system are  $r(\tau = 0) = 0$  and  $i(\tau = 0) = I_b$ . The functions  $\mathcal{L}_k(i)$  and  $v(i)$  are intrinsic functions of the nanowire. Thus, for a specific bias current and nanowire, pulses with different numbers of photons or from detectors of different lengths are described by exactly the same scaled system, even if the kinetic inductance of the detector depends on the current. The solution for this scaled system  $i(\tau)$ ,  $r(\tau)$  is unique and scaling relations for different rise times for pulses of different photon numbers or from detectors with different lengths are found by expressing the scaled solutions in terms of the physical

variables via Eqs. (A3–A5). For example, for two detectors  $A$  and  $B$ ,

$$I_{\text{det}}^A \left( \sqrt{\frac{n_A}{\ell_A}} t \right) = i(\tau) = I_{\text{det}}^B \left( \sqrt{\frac{n_B}{\ell_B}} t \right)$$

$$\Rightarrow I_{\text{det}}^A \left( \sqrt{\frac{n_A \ell_B}{n_B \ell_A}} t \right) = I_{\text{det}}^B(t). \quad (\text{A8})$$

Consequently, the functional shapes of the rising edges of their pulses are mathematically similar in the sense of Eq. (9) and Fig. 2.

## APPENDIX B: EXPERIMENTAL PROCEDURE

To test the theoretical predictions described in the main paper, we perform experiments to measure the rise time of the photon-detection waveforms as a function of  $n$  as well as  $I_{\text{bias}}$ . The detector is a single-pixel meander, made of a proprietary amorphous superconducting material from Quantum Opus [22]. We operate the detector at 850 mK on the cold finger of a  $^4\text{He}$  sorption refrigerator made by Chase Research Cryogenics [23], which itself is mounted on the cold finger of a closed-cycle  $^4\text{He}$  refrigerator housed in a custom-built cryostat.

To resolve changes in the rise time of the electrical waveform, we use a low-noise high-bandwidth readout circuit, which is shown in Fig. 6, together with the lumped-element depiction of the SNSPD. The cryogenic preamplifier is a model CITLF3 from Cosmic Microwave Technologies, with a specified analog bandwidth of 10–2000 MHz, a noise temperature of 4 K, and a gain of  $> 30$  dB. An additional amplifier (Mini-Circuits ZFL1000-LN, specified bandwidth 0.1–1000 MHz) at room temperature boosts the signal well above the noise floor of the oscilloscope that we use to collect the waveforms (Agilent Infinium 80404B, 8 GHz analog bandwidth, 40 gigasamples/s). Note that we measure these bandwidths and find the specifications to be conservative. As a result, in Appendix C we use the measured cutoff frequencies.

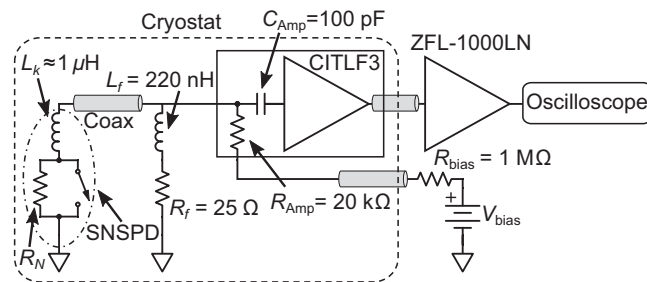


FIG. 6. A schematic of the experimental setup used for collecting the waveform data. The SNSPD is shown as the typical lumped-element depiction with a kinetic inductance  $L_k$  and a hot-spot resistance  $R_N$  that is a function of the absorbed photon number  $n$ .

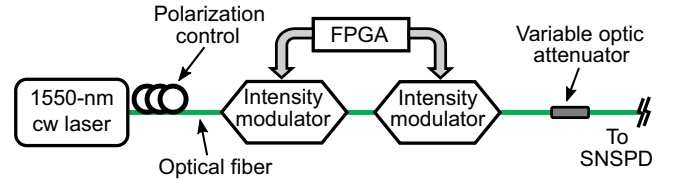


FIG. 7. A schematic of the source setup used in generating multiphoton wave packets.

To mitigate current back-action that affects ac-coupled SNSPD readout circuits [24], we use a passive crossover network at the input to the CITLF3. This network provides a dc path to ground that prevents charging of the input capacitor to the amplifier without degrading the fast rise time of the waveform [25]. Waveforms are recorded at different values for  $I_{\text{bias}}$  and  $n$  using the oscilloscope.

The source consists of a distributed-feedback continuous-wave (cw) laser (Fitel F0L15DCWC-A82-19340-B) operating at 1550 nm that is intensity modulated via electro-optic modulators (EOSpace). The repetition rate and width of the modulation signal are controlled by a field-programmable gate array (FPGA; Altera Stratix V 5SGXEA7N2F40C2), shown in Fig. 7. Two sequential modulators are used to increase the overall extinction ratio between the “ON” and “OFF” states. After creating the pulse with the modulators, it is attenuated to the desired mean photon number per pulse with a variable optical attenuator before traveling to the detector. In the data presented in this paper, the width of the modulated optical pulse is approximately 80 ps, the repetition rate is 610 kHz, and the mean photon number per pulse is approximately 1.26.

## APPENDIX C: EFFECT OF THE FINITE BANDWIDTH OF THE DETECTION SYSTEM

We assume in the main text that the system gain for the SNSPD signal is flat as a function of the frequency and that the bandwidth is infinite. The most significant departure from this in the experimental apparatus is the high frequency limits of our system. The expected decrease in system gain at high frequencies is dominated by the room-temperature amplifier, the gain of which we measure to be down by 3 dB at  $f_{\text{ip}} = 2.4$  GHz. Accordingly, we model the system gain’s high-frequency roll-off by a single-pole low-pass filter with a time constant  $\tau = 2\pi/f_{\text{ip}}$ . Here,  $R$  and  $C$  are chosen to reproduce the amplifier’s 3 dB corner frequency. For this model, the “actual” signal,  $v_{\text{actual}}(t)$  that would be observed for an infinite-bandwidth system is expressed in terms of the measured filtered signal  $v_{\text{measured}}(t)$ :

$$v_{\text{actual}}(t) = \tau \frac{dv_{\text{measured}}(t)}{dt} + v_{\text{measured}}(t). \quad (\text{C1})$$

The derivative signal in Fig. 2 shows this effect most clearly. The peak heights are inversely proportional to the pulse rise times and the finite bandwidth of the system means that the measured heights of these curves will be somewhat smaller than the “actual” heights that result from amplifiers with infinite bandwidth. We mathematically model the “measured” curves as Gaussians with the full-width-at-half-maximum values taken from the data shown in the figure. Using Eq. (C1), we predict that for events of one, two, and three photons, the “actual” peaks are reduced by 6%, 11%, and 15%, respectively, to give those measured values in the figure. Equivalently, the actual lifetimes are expected to be shorter than the measured rise times by the same amounts, according to this model of the system’s frequency dependence. This size of an effect is right at the edge of our experimental sensitivity, given uncertainties in the exact shape of the pulse rise-time distributions, and we do not identify it in our data. Future higher-precision work and, especially, an extension of this technique to higher-photon-number events, will require care on this score.

#### APPENDIX D: COMPARISON OF RAW WAVEFORMS TO RESCALED WAVEFORMS FOR DIFFERENT $n$

To determine whether there is a statistical significance between the waveforms shown in Fig. 2 of the main text, we perform a one-way ANOVA [26] on the derivative waveforms at  $t = 0$ . Typical one-way ANOVA results are reported using an  $F$ -statistic, which represents the ratio of the variance between groups to the variance within groups as a function of degrees of freedom between the groups and the total degrees of freedom, and a  $p$ -value representing the significance level, where  $p < 0.05$  is considered to be statistically significant. For the raw waveforms, the results are  $F(2, 12) = 140$ ,  $p = 5.6 \times 10^{-9}$ , which shows a statistically significant difference. *Post hoc* comparisons using the Tukey HSD test show a significant difference between the  $n = 1$  and  $n = 2$ ,  $n = 2$  and  $n = 3$ , and  $n = 1$  and  $n = 3$  groups. In contrast, for the rescaled waveforms, we find  $F(2, 12) = 1.7$ ,  $p = 0.22$ , indicating no statistical significance between the waveforms at  $t = 0$ .

#### APPENDIX E: DIGITIZATION AND FITTING OF SMIRNOV DATA

The data used to compare the Smirnov *et al.* two-temperature predictions with our theory are digitized from Ref. [15] using the PLOT DIGITIZER software [27]. As described in the main text, our theory agrees well with theirs, with  $\chi_r^2 \sim 1$ , and agrees qualitatively with their experimental findings. When calculating  $\chi_r^2$ , we assume that the dominant error is the approximately 1.6 ps error introduced by digitizing. The digitization program works

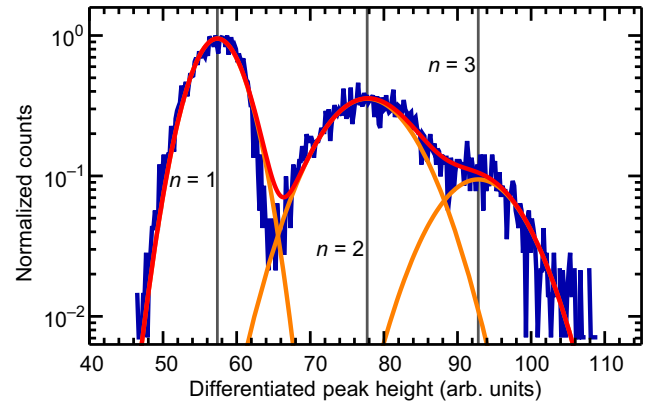


FIG. 8. A histogram of the differentiated peak heights (blue) for  $I_b = 11 \mu\text{A}$ . We fit a sum of Gaussian functions (red) of the form  $\sum_{n=1}^3 a_n e^{-[(x-b_n)/c_n]^2}$  to the distribution. The resulting individual Gaussians (orange curves) and their centers (gray vertical lines) are also shown.

by allowing the user to set the axes and hand-select data points to record their values. We arrive at this digitization error by selecting the same data point multiple times.

#### APPENDIX F: EXTRACTING $t_{\text{ch}}$ FROM EXPERIMENTAL PULSES

To arrive at values for  $t_{\text{ch}}$  for varying  $n$ , we follow Ref. [6] and make a histogram of the maximum values of the derivatives of readout pulses as shown in Fig. 8. We fit a sum of Gaussians to the distribution, finding that  $\chi_r^2 \sim 2.2$ , and then use each Gaussian’s center to determine representative pulses for  $n=1, 2$ , and 3. We then fit these representative pulses using our universal  $t$  model [Eq. (11)]

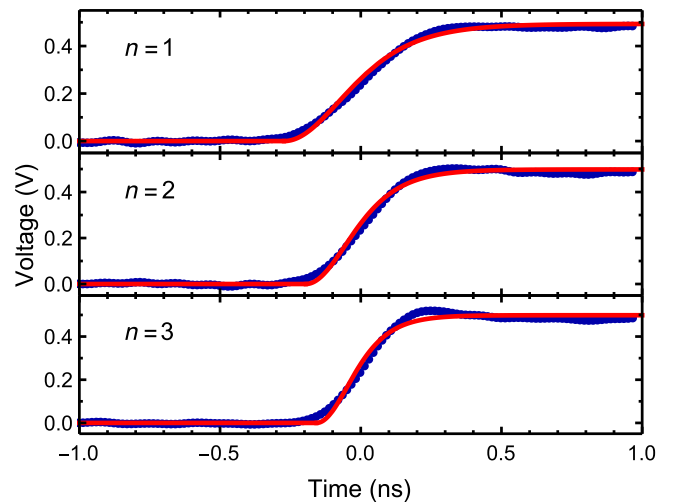


FIG. 9. The universal model fits (red solid line) for  $n = 1, 2$ , and 3 (blue points).



TABLE I. The values of  $t_{\text{ch}}$  found by fitting the universal model solution to experimental waveforms.

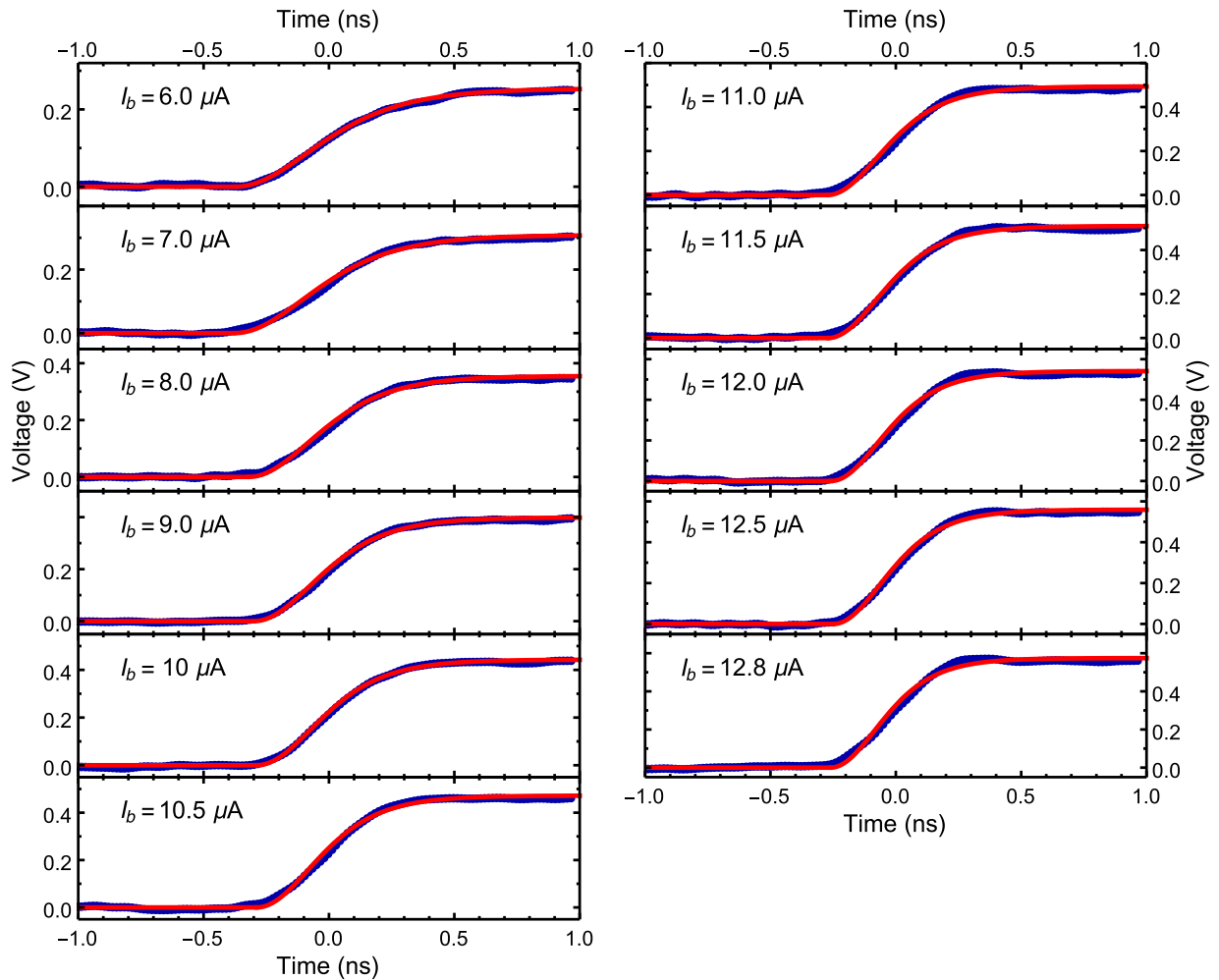
$n$	$I_b$ ( $\mu\text{A}$ )	$t_{\text{ch}}$ (ns)
1	12.8	$0.264 \pm 0.007$
1	12.5	$0.275 \pm 0.005$
1	12.0	$0.276 \pm 0.007$
1	11.5	$0.287 \pm 0.006$
1	11.0	$0.294 \pm 0.007$
2	11.0	$0.212 \pm 0.006$
3	11.0	$0.166 \pm 0.006$
1	10.5	$0.310 \pm 0.006$
1	10.0	$0.323 \pm 0.004$
1	9.0	$0.335 \pm 0.004$
1	8.0	$0.358 \pm 0.006$
1	7.0	$0.409 \pm 0.008$
1	6.0	$0.429 \pm 0.007$

to determine  $t_{\text{ch}}$ , as shown in Fig. 9. The resulting values are given in Table I. Note that with a value of  $t_{\text{ch}}$  extracted in this manner for a pulse with a known  $n$ , combined with

a measurement of  $L_k$  as described below, it is possible to extract  $R_{\text{ch}}$  as well.

For varying  $I_b$ , we use the same procedure and focus only on the  $n = 1$  peak for each value of  $I_b$ . Fits to the waveforms can be found in Fig. 10 and values of  $t_{\text{ch}}$  are given in Table I.

The  $\chi_r^2$  value for these fits ranged from 1.1 to 11.5 for  $I_b = 6\text{--}12.8 \mu\text{A}$ , and from 6.6 to 14.1 for  $n = 1, 2$ , and 3. We hypothesize that the increase of  $\chi_r^2$  is due in part to the limited bandwidth of, and the ringing behavior observed in, our amplifier. The rising edge for  $n = 3$  and  $I_b = 12.8 \mu\text{A}$  is somewhat faster than the amplifier rise time and therefore the fit slightly underestimates the actual data when the pulse first begins to rise at approximately  $-0.15$  ns. Similarly, when the pulse begins to round off at its maximum value at approximately 0.2 ns, the amplifier rings, again causing the fit to somewhat undershoot the actual data. This effect should be more pronounced for higher  $n$  and  $I_b$ , where the rise time is shortest, and this is reflected in the higher  $\chi_r^2$  for these fits.


 FIG. 10. The universal model fits (red solid line) for different values of  $I_b$  (blue points).

## APPENDIX G: DETERMINING DETECTOR PARAMETERS

### 1. Steady state current

The steady-state current  $I_{ss}$  is defined as the current when the Joule heating and cooling to the substrate are balanced such that  $v(I_{ss}) = 0$ . We determine  $I_{ss}$  by performing a dc current-voltage ( $I$ - $V$ ) measurement as shown in Fig. 11. We start with a high voltage such that the whole meander is in the normal state. We gradually lower the voltage and observe a plateau region starting at around 6 V and ending at around 1 V. In this region, sections of the nanowire are beginning to switch into the superconducting state, causing the resistance to drop. In turn, the current maintains a constant value,  $I_{ss}$ . We fit a line to the  $I$ - $V$  curve from 4 to 6 V and find that the vertical offset is  $I_{ss} = 1.042 \pm 0.005 \mu\text{A}$ .

### 2. Kinetic inductance

To determine  $L_k$ , we model the electrical properties of the SNSPD during the falling edge of the readout pulse and fit to the experimental waveforms. We place the detector in parallel with two room-temperature amplifiers using a bias tee (Mini-Circuits ZFBT-6GW). Typically, it is assumed

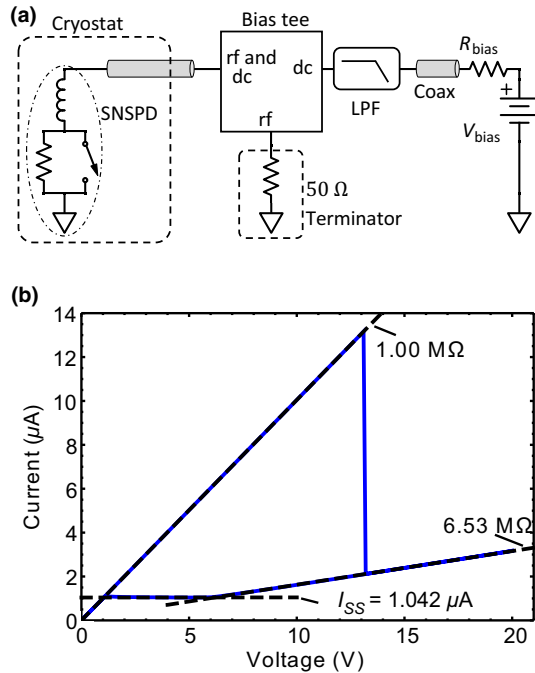


FIG. 11. The measurement schematic (a) and the resulting  $I$ - $V$  curve (b) for the Quantum Opus detector. There is a  $1 \text{ M}\Omega$  series resistor  $R_{\text{bias}}$  between the voltage source and the detector, resulting in a slope of  $1 \text{ M}\Omega$  during the superconducting portion of the  $I$ - $V$  curve. The normal resistance is about  $6.53 \text{ M}\Omega$  including  $R_{\text{bias}}$ . The bias tee is a Mini-Circuits ZFBT-6GW and the low-pass filter (LPF) is a Mini-Circuits SLP-1.9+.

that the fall time for  $I_s$  is given by  $\tau_r = L_k/R_L$ . In this case, we modify this assumption to also allow for timing variations caused by the ac-coupling capacitor. We use the following model:

$$I_s(t) = e^{(R_L/2L_k)(t-t_o)} \left[ ae^{\sqrt{(R_L/2L_k)^2 - 1/(L_k C)}(t-t_o)} + be^{-\sqrt{(R_L/2L_k)^2 - 1/(L_k C)}(t-t_o)} \right], \quad (\text{G1})$$

where  $R_L = 50 \Omega$  and  $a$ ,  $b$ ,  $t_o$ ,  $L_k$ , and  $C$  are left as free parameters. ( $C$  is not specified by the bias-tee manufacturer, so we allow it to be a fit parameter.) We fit Eq. (G1) to the pulse shown in Fig. 12 from  $t \sim 15 \text{ ns}$  to  $t = 250 \text{ ns}$ . We find that  $a = -0.059 \pm 0.004 \text{ V}$ ,  $b = 1.53 \pm 0.01 \text{ V}$ ,  $t_o = -1.2722 \pm 0.0004 \text{ ns}$ ,  $C = 3.2 \pm 0.2 \text{ nF}$ , and  $L_k = 824 \pm 4 \text{ nH}$ . The fit has  $\chi_r^2 \sim 1.6$ .

### 3. Dark counts

The dark-count rate (DCR), as well as the total count rate (TCR) as a function of  $I_b$  for the detector, are shown in Fig. 13. At higher  $I_b$  ( $\gtrsim 11 \mu\text{A}$ ), the DCR grows to within 2 orders of magnitude of the TCR.

Careful analysis of our dark counts reveals an interesting phenomenon, which is not accounted for by our model. We collect dark-count pulses, differentiate their rising edges, and record their maximum derivatives in the

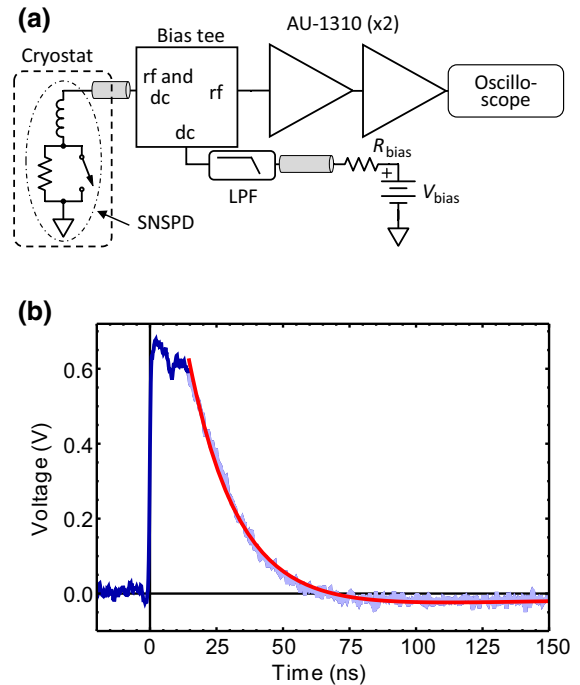


FIG. 12. The measurement schematic (a) and the resulting SNSPD pulse (b). We fit Eq. (G1) (red) to the falling edge (light blue region) and extract  $L_k$ . The low-pass filter (LPF) is a Mini-Circuits SLP-1.9+.

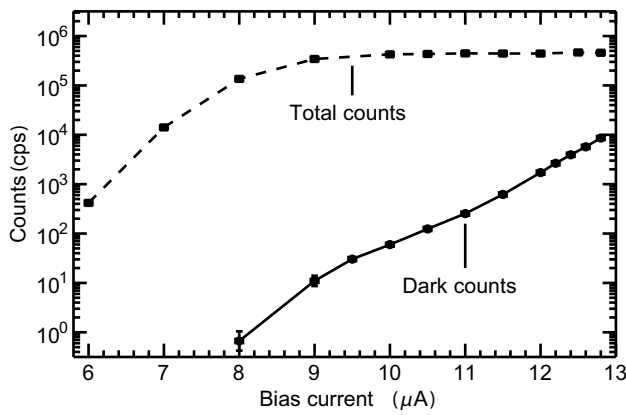


FIG. 13. The detector dark-count rate (points with solid line) varies from a few counts per second (cps) for low  $I_b$  up to  $> 8000$  cps for high  $I_b$ . The total count rate (squares with dotted line) is also shown. (Note that the measured results are given by the plot points—the lines are just guides for the eye.)

same way as above. We assume that we do not obtain any multiphoton dark-count events and so the resulting distribution represents only  $n = 1$  counts. We compare the resulting distribution with our multiphoton distribution and find that the  $n = 1$  dark counts are shifted to a lower-differentiated peak height (a longer rise time) as shown in Fig. 14. A possible explanation for this shift is that the dark-count photons are likely of much longer wavelength than our source photons [28]; however, there is no mechanism in our model to account for this proposed difference. This is an important issue that warrants further exploration.

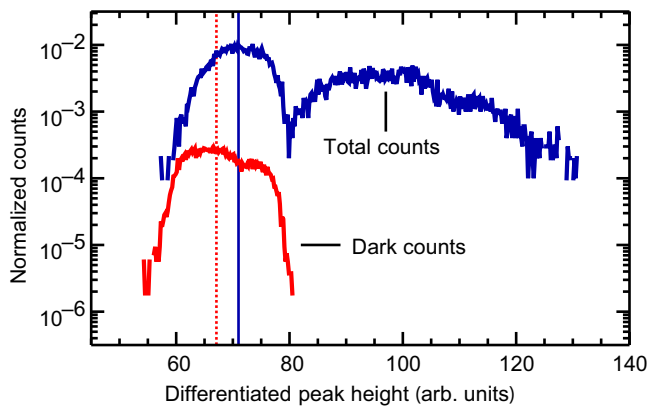


FIG. 14. A comparison of the multiphoton absorption data (blue) with the dark-count rates (red) at  $I_b = 12.8 \mu\text{A}$ . Both distributions are normalized such that the areas under their curves are unity, then the dark counts are further scaled by the ratio of the DCR over the overall count rate during data collection. Gaussians are fitted to the  $n = 1$  peak and their centers are shown as vertical lines for both source (solid blue) and dark (dotted red) counts.

- [1] E. A. Dauler, M. E. Grein, A. J. Kerman, F. Marsili, S. Miki, S. W. Nam, M. D. Shaw, H. Terai, V. B. Verma, and T. Yamashita, Review of superconducting nanowire single-photon detector system design options and demonstrated performance, *Opt. Eng.* **53**, 081907 (2014).
- [2] R. H. Hadfield and G. Johansson, eds., *Superconducting Devices in Quantum Optics* (Springer, New York, 2015).
- [3] A. Engel, J. Renema, K. Il'in, and A. Semenov, Detection mechanism of superconducting nanowire single-photon detectors, *Supercond. Sci and Tech.* **28**, 114003 (2015).
- [4] J. K. W. Yang, A. J. Kerman, E. A. Dauler, V. Anant, K. M. Rosfjord, and K. K. Berggren, Modeling the electrical and thermal response of superconducting nanowire single-photon detectors, *IEEE Trans. Appl. Supercond.* **17**, 581 (2007).
- [5] A. J. Kerman, J. K. W. Yang, R. J. Molnar, E. A. Dauler, and K. K. Berggren, Electrothermal feedback in superconducting nanowire single-photon detectors, *Phys. Rev. B* **79**, 100509(R) (2009).
- [6] C. Cahall, K. L. Nicolich, N. T. Islam, G. P. Lafyatis, A. J. Miller, D. J. Gauthier, and J. Kim, Multi-photon detection using a conventional superconducting nanowire single-photon detector, *Optica* **4**, 1534 (2017).
- [7] J. R. Clem and V. G. Kogan, Kinetic impedance and depairing in thin and narrow superconducting films, *Phys. Rev B* **86**, 174521 (2012).
- [8] L. N. Bulaevskii, M. J. Graf, and V. G. Kogan, Vortex-assisted photon counts and their magnetic field dependence in single-photon superconducting detectors, *Phys. Rev. B* **85**, 014505 (2012).
- [9] J. J. Renema, R. Gaudio, Q. Wang, Z. Zhou, A. Gaggero, F. Mattioli, R. Leoni, D. Sahin, M. J. A. de Dood, A. Fiore, and M. P. van Exter, Experimental Test of Theories of the Detection Mechanism in a Nanowire Superconducting Single Photon Detector, *Phys. Rev. Lett.* **112**, 117604 (2014).
- [10] A. Casaburi, R. M. Heath, M. Ejrnaes, C. Nappi, R. Cristiano, and R. H. Hadfield, Experimental evidence of photoinduced vortex crossing in current carrying superconducting strips, *Phys. Rev. B* **92**, 214512 (2015).
- [11] A. Engel, J. Lonsky, X. Zhang, and A. Schilling, Detection mechanisms in SNSPD: Numerical results of a conceptually simple, yet powerful detection model, *IEEE Trans. Appl. Supercond.* **25**, 2200407 (2015).
- [12] R. Gaudio, J. J. Renema, Z. Zhou, V. B. Verma, A. E. Lita, J. Shainline, M. J. Stevens, R. P. Mirin, S. W. Nam, M. P. van Exter, M. J. A. de Dood, and A. Fiore, Experimental investigation of the detection mechanism in WSi nanowire superconducting single photon detectors, *Appl. Phys. Lett.* **109**, 031101 (2016).
- [13] A. D. Semenov, G. N. Gol'tsman, and A. A. Korneev, Quantum detection by current carrying superconducting film, *Phys. C* **351**, 349 (2001).
- [14] D. Hazra, L. Pascal, H. Courtois, and A. K. Gupta, Hysteresis in superconducting short weak links and  $\mu$ -squids, *Phys. Rev. B* **82**, 184530 (2010).
- [15] K. Smirnov, A. Divochiy, Y. B. Vakhtomin, M. Sidorova, U. Karpova, P. Morozov, V. Seleznev, A. Zotova, and D. Y. Vodolazov, Rise time of voltage pulses in NbN

- superconducting single photon detectors, *Appl. Phys. Lett.* **109**, 052601 (2016).
- [16] C. M. Natarajan, M. G. Tanner, and R. H. Hadfield, Superconducting nanowire single-photon detectors: Physics and applications, *Supercond. Sci. Technol.* **25**, 063001 (2012).
- [17] A. V. Gurevich and R. G. Mints, Self-heating in normal metals and superconductors, *Rev. Mod. Phys.* **59**, 941 (1987).
- [18] R. F. Broom and E. H. Rhoderick, Thermal propagation of a normal region in a thin superconducting film and its application to a new type of bistable element, *Br. J. Appl. Phys.* **11**, 292 (1960).
- [19] K. K. Berggren, Q.-Y. Zhao, N. Abebe, M. Chen, P. Ravindran, A. McCaughan, and J. C. Bardin, A superconducting nanowire can be modeled by using SPICE, *Supercond. Sci. Technol.* **31**, 055010 (2018).
- [20] D. F. Santavica, J. K. Adams, L. E. Grant, A. N. McCaughan, and K. K. Berggren, Microwave dynamics of high aspect ratio superconducting nanowires studied using self-resonance, *J. Appl. Phys.* **119**, 234302 (2016).
- [21] K. L. Nicolich, C. T. Cahall, G. P. Lafyatis, J. Kim, D. J. Gauthier, M. Allman, V. Verma, and S. W. Nam, in *Single Photon Workshop 2017, Boulder, CO, Jul. 31–Aug. 4* (2017).
- [22] Quantum Opus, <https://www.quantumopus.com/web/> (last accessed on 2018-10-01).
- [23] Chase Research Cryogenics, <http://www.chasecryogenics.com/> (last accessed on 2018-10-01).
- [24] A. J. Kerman, D. Rosenberg, R. J. Molnar, and E. A. Dauler, Readout of superconducting nanowire single-photon detectors at high count rates, *J. Appl. Phys.* **113**, 144511 (2013).
- [25] C. Cahall, D. J. Gauthier, and J. Kim, Scalable cryogenic readout circuit for a superconducting nanowire single-photon detector system, *Rev. Sci. Instrum.* **89**, 063117 (2018).
- [26] W. Navidi, *Statistics for Engineers and Scientists* (McGraw Hill, 2007), 2nd ed.
- [27] Plot Digitizer, <http://plotdigitizer.sourceforge.net/> (last accessed on 2018-10-01).
- [28] H. Shibata, K. Shimizu, H. Takesue, and Y. Tokura, Ultimate low system dark-count rate for superconducting nanowire single-photon detector, *Opt. Lett.* **40**, 3428 (2015).